

Natural Spinors Reveal How the Spin–Orbit Coupling Affects the Jahn–Teller Distortions in the Hexafluorotungstate(V) Anion

Tao Zeng,^{†,||} Dmitri G. Fedorov,[‡] Michael W. Schmidt,[§] and Mariusz Klobukowski^{*,†}

[†]Department of Chemistry, University of Alberta, Edmonton, AB T6G 2G2, Canada

[‡]NRI, National Institute of Advanced Industrial Science and Technology (AIST), Central 2, Umezono 1-1-1, Tsukuba, 305-8568, Japan

[§]Department of Chemistry and Ames Laboratory USDOE, Iowa State University, Ames, Iowa 50011, United States

ABSTRACT: We investigate the Jahn–Teller distortions in the hexafluorotungstate(V) anion (WF_6^-) by applying the recently developed concept of natural spinors (spin–orbitals) and show that they are a very powerful tool providing simple and clear pictorial explanation for the spin–orbit effect in determining the structure of the anion. The calculations are performed at the levels of spin–orbit configuration interaction and multiconfigurational quasi-degenerate perturbation theory. The hexafluorotungstate(V) anion represents a very rare example of spin–orbit coupling enhancing the Jahn–Teller distortion, and the natural spinor analysis gives a clear interpretation of this enhancement. Advantages of using the natural spinors are explored and explained in detail in this case study.

■ INTRODUCTION

Tungsten hexafluoride (WF_6), one of the heaviest known gases under standard conditions,¹ plays a very important role in the semiconductor industry. Its extraordinarily high conformity of chemical vapor deposition of tungsten makes the “tungsten plug” process possible.^{2–5} Despite its importance in industry, there was no high level quantum chemistry study for this species before 2000. Dyllal⁶ carried out the first study to calculate its bond dissociation energy, ionization potential, and electron affinity using density functional theory. He also investigated the lower-order tungsten fluorides (WF_n with $n < 6$) which form as intermediates in WF_6 formation. However, after this work, this molecule faded from the vision of quantum chemists, as, although Dyllal’s pioneering paper had been cited 12 times (according to ISI Web of Knowledge), only one electronic structure study on this species followed recently.⁷ In short, the number of theoretical studies of WF_6 and its derivatives is not commensurate with its industrial importance, and more detailed studies are desirable. For heavy d-block elements, such as tungsten, the spin–orbit effect is substantial and may be a determining influence on the structure of its compounds.^{8–11} The spin–orbit coupling is very important for open-shell systems with electronic degeneracy,^{9,12–14} and Dyllal⁶ employed a simple model to estimate this coupling. In recent years, there has been remarkable progress in *ab initio* and semiempirical spin–orbit computations,^{8,9,14–16} and at present, accurate calculations on the spin–orbit coupling have become routine. Therefore, WF_6 should be re-examined using new methods for higher level spin–orbit calculations. We recently developed an algorithm¹⁷ to define the natural spin–orbitals (natural spinors) from the two-step SO coupled^{18–23} wave function and found that those natural spinors are very effective in explaining the SO quenching of the JT effect in WF_5 .²⁴ We expect that this novel algorithm will also be a powerful tool to examine WF_6 . Indeed, we discover new features and utilities of the natural spinors in the present study, and thus this work should not be considered as a simple follow-

up application of the new concept by a case study. Rather, it is a theoretical contribution to the community of quantum chemistry. Note that in the present paper the term “spinor” is reserved for the relativistic spinors which couple the α and β electronic spin orbitals through the SO effect. They should not be mistaken as the simple products of spatial and spin orbitals.

The ground electronic state of WF_6 was determined to belong to the 1A_g irreducible representation (irrep) of the O_h point group.⁶ This spatially and spin nondegenerate term symbol determines that the molecule is exempt from the Jahn–Teller (JT)^{25–27} and first-order spin–orbit coupling (SOC) effects. Therefore, WF_6 should maintain the typical octahedral structure of ML_6 molecules. The highest occupied molecular orbital (HOMO) of WF_6 is a degenerate t_{1g} orbital composed of the 2p orbitals on fluorines, whose spin–orbit (SO) interaction is too weak to influence the structure of the WF_6^+ cation, so the cation undergoes JT distortion as in the spin-free (no SOC) case.⁶ The lowest unoccupied molecular orbital (LUMO) of WF_6 , however, is a degenerate t_{2g} orbital mainly composed of the 5d orbital of tungsten, which has a strong SOC and may lead to JT distortions different than for the spin-free case. For this reason, in the present work we focus our attention on the hexafluorotungstate(V) anion (WF_6^-) to examine the interplay between SOC and JT effects in determining the structure of the ion. The large electron affinity of WF_6 (found to be within the range of 3.5–3.7 electron volts (eV))^{28–31} leads to facile formation of WF_6^- . There have been many examples of the stable existence of the ionic hexafluorotungstate(V) salts, formed mainly with alkali metals.^{32,33}

A theoretical study on this species will be helpful for future inorganic chemistry investigations. As shown in the present study, the JT effect in WF_6^- is *not* quenched by the SOC effect, and we use natural spinors to explain this observation, providing

Received: March 9, 2012

Published: July 31, 2012

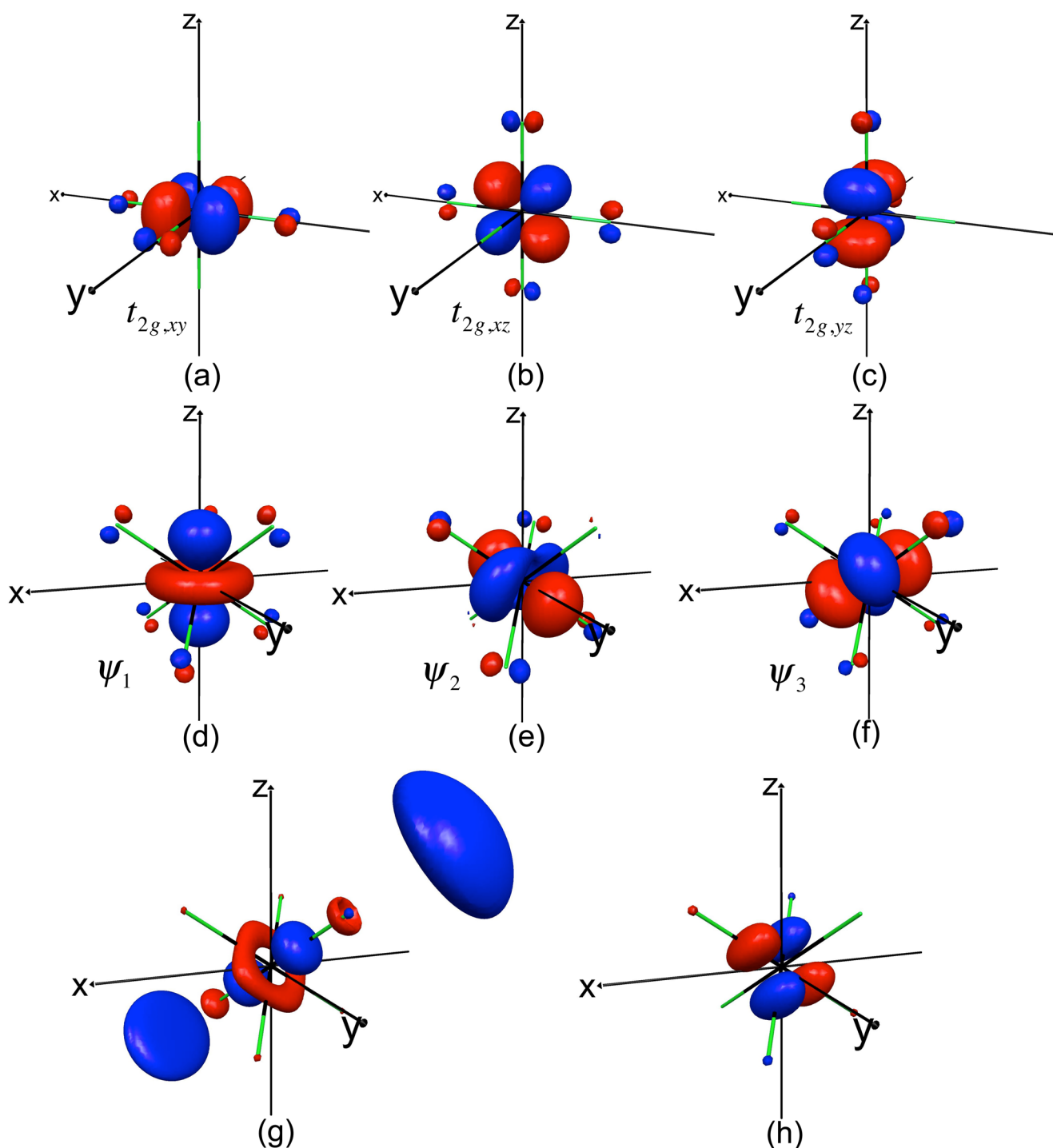


Figure 1. Molecular orbital diagrams. Panels a–c display the t_{2g} orbitals (LUMO of WF_6 ; the natural orbitals of WF_6^- are essentially identical) taking the standard O_h or D_{4h} orientation. Panels d–f show the recombination of a–c in the D_{3d} orientation. Panels g and h illustrate the virtual orbitals with a substantial tungsten d character. In the O_h or D_{4h} orientation, the orbitals in g and h have the $d_{2z^2-x^2-y^2}$ and $d_{x^2-y^2}$ character, respectively. g and h are plotted in the D_{3d} orientation here. Fluorines are indicated by the green color, and tungsten is at the origin in all coordinate systems.

a case study for future applications of this technique. For more recent research on the spin–orbit JT effect, the reader is referred to the elegant papers^{34–39} from Domcke’s group and to the Alvarez-Thon et al. study⁴⁰ on the octahedral structure of PtF_6 .

The present paper is arranged as follows. In the Methodology section, the computational details are given together with a brief review of the natural spinor methodology. In the Results and Discussion, we employ the natural orbitals and natural spinors of WF_6^- to rationalize the possible JT distortion modes without and

with the SOC effects. The potential energy surfaces (PESs) are calculated to justify the rationalization. The Conclusions section summarizes the present study.

METHODOLOGY

For the heavy element tungsten, the effective core potential (ECP) of Stevens, Basch, Krauss, Jasien, and Cundari (SBKJC)^{41–43} is used, with its associated 4111 split L-shell and 311 split D-shell basis set. The scalar-relativistic effect is treated at

the Wood-Boring level⁴⁴ in this ECP, and its basis set is more flexible than the double- ζ basis (LANL2DZ)⁴⁵ used by Dyall. As shown in the discussion below, WF_6 possesses a significantly ionic nature, and tungsten is typically electron-deficient. Thus, no extra diffuse and polarization functions are added for tungsten. The aug-cc-pVDZ⁴⁶ basis set of Dunning is used for fluorine. This basis set is of 3s2p1d quality, augmented with 1s1p1d diffuse functions. The same fluorine basis set was used by Dyall,⁶ and its augmented diffuse functions can satisfactorily describe the electron-rich nature of fluorine centers. The electron correlation is treated at the levels of the complete active space configuration interaction (CASSCI) method and multiconfigurational quasi-degenerate perturbation theory (MCQDPT).^{47–49} The corresponding SOC methods, SO-CASSCI⁵⁰ and SO-MCQDPT,⁵¹ are employed when SOC is considered. Koseki's SOC adapted effective charge⁵² is used for tungsten, and correspondingly, the one-electron Pauli SOC operator is used. To avoid the intruder state problem, the default level-shift parameter of 0.02 was used for the MCQDPT calculations and 0.1 for the SO-MCQDPT calculations.^{53,54}

In the present work, we employ only a limited active space generated by distributing one electron in three orbitals (see below) for CAS self-consistent field (CASSCF) and SOC calculations. These small CASSCF calculations amount to open-shell SCF calculations which enforce the desired orbital degeneracies through state-averaging. Because of the lack of analytical gradients for the SOC operator in our program, we have to scan the PES on a grid to locate the energetic minima, so a compromise between computational efficiency and accuracy is needed. The molecular orbitals are CASSCF optimized at each grid point of the PES and used for the subsequent SOC calculations. For all structures distorted from the octahedral geometry, in the CASSCF calculations we equally average the three closely lying states stemming from the ${}^2T_{2g}$ term of WF_6^- , as the SO interaction couples those states and they need to be treated equally. Throughout this work, we adopt the usual notation, with the lower case symbols used to label one-electron orbitals or spinors while the upper case symbols used for the multielectron states. Lower case symbols are also used to label normal vibrational modes. Unless otherwise specified, atomic units (au) are used. In contrast to other JT-SOC papers (e.g., refs 36 and 37), we do not calculate the vibronic coupling constants, as our objective is to look into the problem from the perspective of orbital interaction, which is the common language in the chemistry community. This view is substantiated by a compelling statement, "orbitals provide a natural language for an aufbau of the complex reality of the molecules of the inorganic and organic world."⁵⁵

Natural spinors are a recent concept, which is an extension of the natural orbitals from the spin-free to SO coupled wave functions: the natural spinors are obtained by diagonalizing the SO coupled one-electron reduced density matrix.¹⁷ Properly averaging all of the degenerate levels in the construction of the density matrix leads to the symmetry-adapted natural spinors that can be used to analyze wave functions. The utility of such spinors lies in the fact that one can carry out a SOC wave function analysis based on one-electron functions (like orbitals for spin-free wave functions); furthermore, because the natural spinors are expressed as linear combinations of the orbitals from spin-free calculations, they directly reflect the SO-induced changes in the wave function. The details of this method and some examples of its application in explaining the interplay between SO and bonding effects and the SOC quenching of the JT distortion are

given in an earlier publication.²⁴ An important notion in this work is what we call the electron rotation between orbitals. By this somewhat classical sounding terminology, we mean that the SOC ($\hat{l} \cdot \hat{s}$) causes the electron transfer from one orbital to another, and these two orbitals must have a nonzero matrix element with the angular momentum operator \hat{l} . In order to understand this notation, one has to keep in mind that the angular momentum operator is the rotation generator,⁵⁶ and SOC is essentially realized through electron rotation (see section 1.3.3 of ref 57 for a detailed discussion). This notion is very close to the one used by Turro et al.⁵⁸ All calculations were performed using the program package GAMESS-US,^{59,60} and all the orbital, spinor, and vibrational mode figures were prepared using MacMolPlt.⁶¹

RESULTS AND DISCUSSIONS

Possible Jahn–Teller Active Modes without Considering Spin–Orbit Coupling. In order to find a starting structure for the subsequent study, we first optimized the WF_6 geometry using the second order Møller-Plesset perturbation theory (MP2)⁶² and located the stationary structure with a W–F bond length of 1.852 Å. This value is close to the experimental value of 1.833 Å⁶³ determined by electron diffraction, indicating our methods are qualitatively or semiquantitatively accurate. The population analysis in this MP2 calculation shows that the Mulliken and Löwdin charges on tungsten are 3.15 and 2.58 atomic units (au), respectively, indicating a significant ionic nature for this compound. This strong cationic character of tungsten also indicates that even when an extra electron is placed in the LUMO centered at tungsten to form WF_6^- , diffuse functions are still not needed. This conjecture is confirmed by the 3.67 Mulliken and 2.56 Löwdin charges on tungsten of WF_6^- at the CASSCF level. Note that these charges should not be compared with the aforementioned charges of the neutral WF_6 , since they are obtained at different levels of theory.

The triply degenerate LUMO of WF_6 is shown in Figure 1a–c, and the dominance of tungsten's 5d character is obvious. This dominance confirms the ionic nature of the compound, and because these orbitals resemble the d orbitals, we call the three orbitals in Figure 1a–c $t_{2g,xy}$, $t_{2g,xz}$ and $t_{2g,yz}$, respectively. However, one should keep in mind that they are not pure d orbitals from tungsten, each containing a small antibonding contribution from fluorine. The orbitals with the $d_{2z^2-x^2-y^2}$ and $d_{x^2-y^2}$ dominance (Figure 1g–h) have higher orbital energies. This suggests that the d orbitals are mostly unoccupied and the electron configuration of tungsten in WF_6 is approximately $6s^25d^0$. As the extra electron of WF_6^- occupies one of the $t_{2g,xy}$, $t_{2g,xz}$ and $t_{2g,yz}$ orbitals, the natural orbitals of the anion look similar and so are not depicted separately. The multiconfigurational self-consistent field (MCSCF) geometry optimization with equal averaging of the three states in WF_6^- gives a W–F bond length of 1.892 Å. This octahedral configuration is the CASSCI structure without the JT distortion, and the CASSCI JT stabilization energies (E_{JT}) below are relative to the energy of this structure. The corresponding MCQDPT bond length is calculated to be 1.909 Å. Likewise, the MCQDPT energy of this octahedral configuration is the reference energy for the MCQDPT E_{JT} below. A longer W–F bond length in the anion compared to the neutral species indicates that there is a repulsive interaction between the density distribution of the extra electron at the tungsten center with the negatively charged fluorines; it will be shown below that the directional electrostatic repulsion

between the extra electron on W and the negatively charged F is the origin of the JT distortions.

The geometry of the t_{2g} natural orbital suggests the JT distortion mode of the anion. If the extra electron occupies the $t_{2g,xy}$, then this electron distribution will push the equatorial fluorines (those in the x - y plane; this notation of “equatorial” is used throughout) away. The equatorial fluorines that were pushed away would then exert smaller electrostatic repulsion on the axial ones (those on the z axis; this notation of “axial” is used throughout). The overall result of these interactions is that the equatorial W–F bonds are elongated, the axial bonds are shortened, and the anion should have a compressed D_{4h} symmetric structure (Figure 2a) with a $^2B_{2g}$ ground electronic

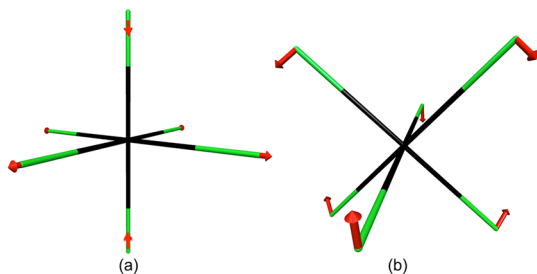


Figure 2. The Jahn–Teller active vibrational modes for a T_{2g} electronic state: (a) e_g mode and (b) t_{2g} mode. The direction shown for each leads to “compressed” geometries.

state (b_{2g} corresponds to $t_{2g,xy}$ in the D_{4h} point group). Because of the symmetry equivalence of the three natural orbitals, the extra electron occupying the $t_{2g,xz}$ or $t_{2g,yz}$ orbital will simply cause similar distortion along different (y or x) axes, and those distortions will not be discussed in detail. This distortion is a component of the typical e_g vibrational mode of an octahedral configuration, and the problem we handle is the typical $T_{2g} \otimes e_g$ problem.²⁶ Reversing the direction of the distortion, i.e., shrinking the equatorial W–F bonds and elongating the axial bonds, makes occupation of the $t_{2g,xy}$ less favorable than for the $t_{2g,xz}$ or $t_{2g,yz}$ because the former has twice the electrostatic repulsive character in the x - y plane than the latter two. Also, the energy increase for the $t_{2g,xz}$ or $t_{2g,yz}$ is compensated by the lowering of their repulsive character on the z axis with the elongation of the axial bonds, and this effect is not available for the $t_{2g,xy}$ orbital. Therefore, the $t_{2g,xz}$ and $t_{2g,yz}$ orbitals remain degenerate at such an elongated D_{4h} structure and have lower energy, resulting in an 2E_g ground electronic state. One should notice that without the SO effect, this 2E_g state undergoes another JT distortion and will finally reach the minima at the

compressed D_{4h} configurations favoring the $t_{2g,xz}$ and $t_{2g,yz}$ occupation (see Figure 3.10 of ref 26). This $T_{2g} \otimes e_g$ problem was already studied by Dyll,⁶ and he predicted a similar D_{4h} structure to be the stable configuration of WF_6^- . However, there is yet another JT active mode.

For a non-SOC degenerate electronic state to have a nonzero JT effect, the irreps of the vibronic operators must be contained in the symmetric direct product of its electronic irrep.^{26,27} For the O_h point group, the symmetric direct product $[T_{2g} \otimes T_{2g}] = A_{1g} \oplus E_g \oplus T_{2g}$, and therefore, there is a t_{2g} JT active mode in addition to the e_g mode discussed above. This mode is illustrated in Figure 2b, and its relation to the d orbitals in Figure 1a–c is not so obvious. The t_{2g} mode in Figure 2b reduces the symmetry of WF_6^- from the O_h to D_{3d} structure, so the relevant analysis will be easier if we reorient the coordinate system to let the z axis be the principal C_3 axis. With such a coordinate, the original $t_{2g,xy}$, $t_{2g,xz}$, and $t_{2g,yz}$ natural orbitals recombine to produce the orbitals illustrated in Figure 1d–f. The orbital in Figure 1d can be easily associated with $d_{2z^2-x^2-y^2}$ in the new coordinates, but the other two cannot be identified easily. Throughout this work, we call the three orbitals ψ_1 , ψ_2 , and ψ_3 , in the order of Figure 1d–f, respectively. The ψ_1 belongs to the A_{1g} irrep, and the other two are the E_g components in the D_{3d} point group. With these three orbitals, the t_{2g} JT active mode is easier to understand. ψ_1 is more protruding along the z axis than on the x - y plane, and this is determined by the $2z^2-x^2-y^2$ Cartesian components of the d orbital. Therefore, bending the W–F bonds toward the x - y plane lowers the electrostatic repulsion between the ψ_1 electron distribution and fluorines and leads to a $^2A_{1g}$ ground state at the compressed D_{3d} structure. The reverse of this distortion (bending the W–F bonds toward the z axis) lowers the repulsion between the ψ_2 (and ψ_3) electron distribution and fluorines, and the 2E_g term would be more stable at the elongated D_{3d} structure. As in the $T_{2g} \otimes e_g$ case, this 2E_g term undergoes another JT distortion in the D_{3d} point group and will finally reach the same minima with the compressed D_{3d} structure by a different route.²⁶ A graphical summary of all of the correlation and coupling schemes of the electronic states under concern under the SOC and JT distortions is given in Figure 3.

The Spin–Orbit Effect. First, we consider the e_g distortion leading to D_{4h} symmetry. In the O_h double group, the electronic spin functions α and β transform as the two components of the $E_{1/2,g}$ irrep, and because of the direct product decomposition $E_{1/2,g} \otimes T_{2g} = G_{3/2,g} \oplus E_{5/2,g}$, the SO interaction splits a $^2T_{2g}$ term into $G_{3/2,g}$ and $E_{5/2,g}$ levels. In this work, we use Jacobs’ notation⁶⁴ to label double group irreps. Dyll suggested that the inclusion of the SO effect would quench the JT distortion because the doubly

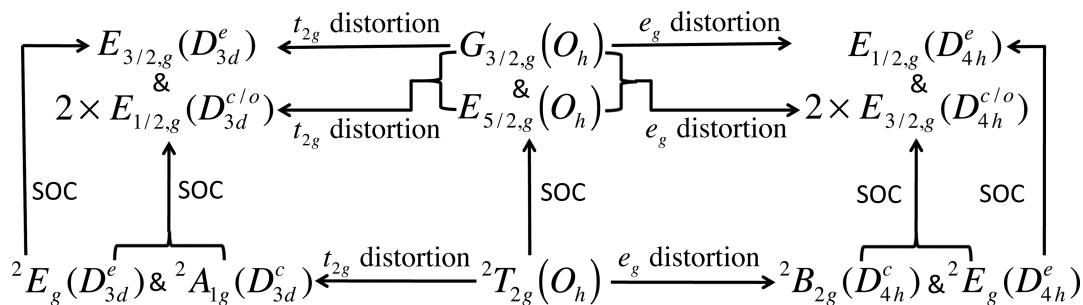


Figure 3. The correlation and coupling scheme of electronic states under SOC and JT distortions. The superscripts “e” and “c” indicate that the electronic state favors the elongated or compressed structure with the group symbol. The superscript “c/o” indicates one of the duplicate states favors the compressed structure, while the other favors the undistorted octahedral structure, correlating to the $E_{5/2,g}$ state.

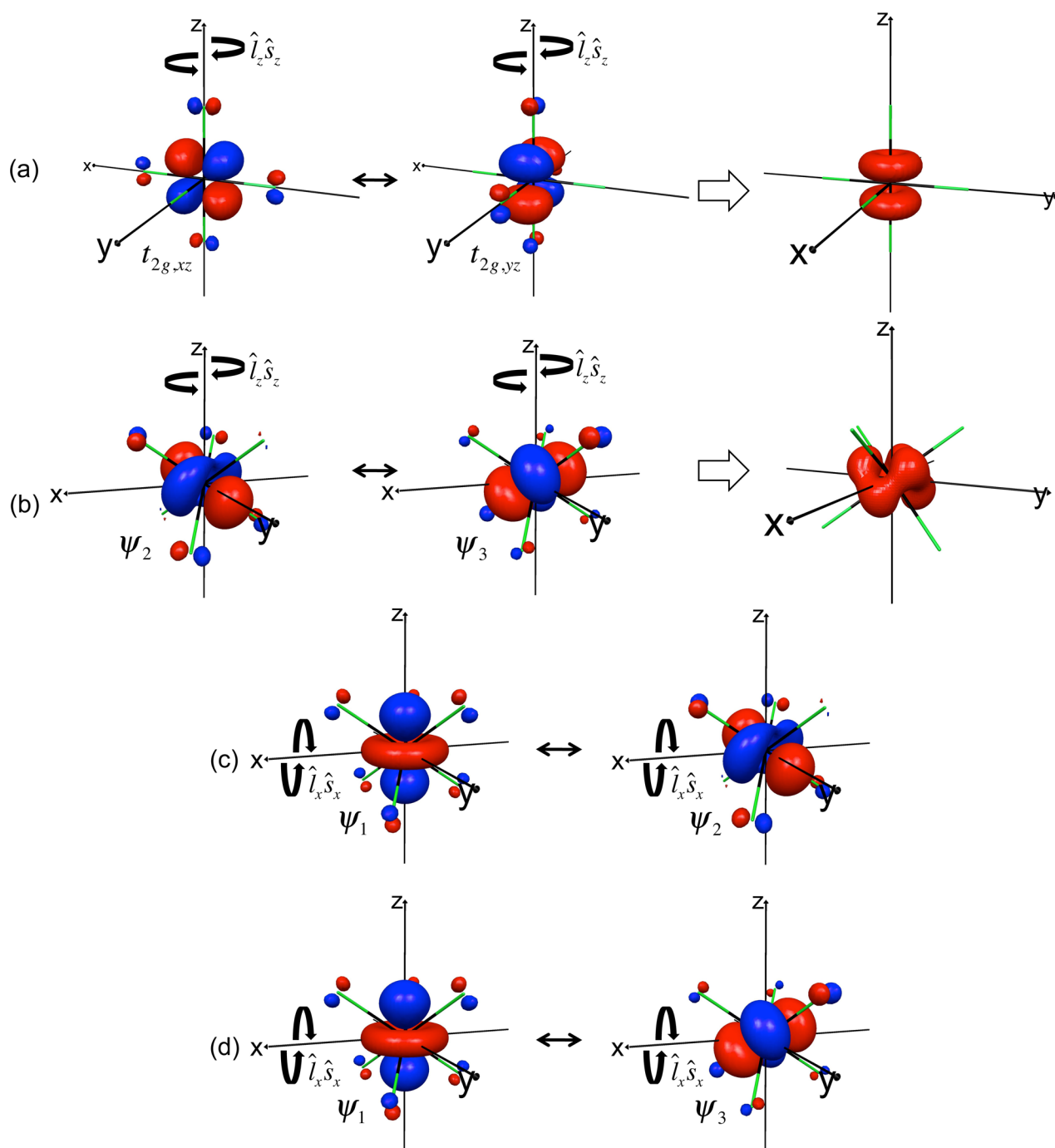


Figure 4. Spin–orbit induced electron rotation: (a) The $\hat{l}_z \hat{s}_z$ induced rotation between the $t_{2g,xz}$ ($e_{g,xz}$) and $t_{2g,yz}$ ($e_{g,yz}$) orbitals creates totally symmetric electron distribution of the natural spinors in the D_{4h} point group. (b) The $\hat{l}_z \hat{s}_z$ induced rotation between ψ_2 (e_{g,ψ_2}) and ψ_3 (e_{g,ψ_3}) orbitals creates totally symmetric electron distribution of the natural spinors in the D_{3d} . (c) The $\hat{l}_x \hat{s}_x$ induced rotation between ψ_1 (a_{1g}) and ψ_2 (e_{g,ψ_2}). (d) The $\hat{l}_x \hat{s}_x$ induced rotation between ψ_1 (a_{1g}) and ψ_3 (e_{g,ψ_3}). The parentheses indicate their corresponding orbitals in the respective distorted structures. The rotation arrows are in pairs because the spin–orbit induced rotation can occur in either direction, depending on the spins, to lower the energy.

degenerate $E_{5/2,g}$ state has a lower energy than the quadruply degenerate $G_{3/2,g}$ state, and the former has equal contributions from the three T_{2g} components, resulting in a totally symmetric electron–nuclei interaction. However, our calculations show the opposite. The SO-CASCI calculation at the O_h structure points to a more stable $G_{3/2,g}$ state, and therefore, the JT distortion for the ground state WF_6^- is possible even when SOC is considered. The SOC splitting between the two levels is 4037 cm^{-1} . Taking

the natural orbitals in Figure 1a–c as the basis functions, the natural spinors are calculated to be

$$g_{3/2,g}(\text{I}) = \sqrt{\frac{1}{2}} t_{2g,xz} \beta + i \sqrt{\frac{1}{2}} t_{2g,yz} \beta \quad (1)$$

$$g_{3/2,g}(\text{II}) = \sqrt{\frac{2}{3}} t_{2g,xy} \beta + i \sqrt{\frac{1}{6}} t_{2g,xz} \alpha - \sqrt{\frac{1}{6}} t_{2g,yz} \alpha \quad (2)$$

$$e_{5/2,g} = \sqrt{\frac{1}{3}} t_{2g,xy} \beta - i \sqrt{\frac{1}{3}} t_{2g,xz} \alpha + \sqrt{\frac{1}{3}} t_{2g,yz} \alpha \quad (3)$$

Here, we list just three of the six natural spinors since the left-overs are their Kramers pairs,⁶⁵ which can be easily obtained by operating the time-reversal operator on the listed spinors.⁶⁶ This convention of listing and analyzing only one component of a Kramers pair is used throughout. Roman numbers are used to number components of the same irrep (g is 4-fold degenerate, and we list only I and II, omitting the other two Kramers pairs). If we neglect the small contributions from fluorines to the natural orbitals and assume the natural orbitals on the right-hand sides of the above equations are pure 5d orbitals from tungsten, i.e., approximating $t_{2g,xy}$ by d_{xy} etc., the natural spinors can be written in the representation of the atomic $j-j$ spinors as

$$g_{3/2,g}(\text{I}) \approx -\sqrt{\frac{3}{5}} d_{3/2,1/2} + \sqrt{\frac{2}{5}} d_{5/2,1/2} \quad (4)$$

$$g_{3/2,g}(\text{II}) \approx \sqrt{\frac{3}{5}} d_{3/2,3/2} - \sqrt{\frac{1}{15}} d_{5/2,3/2} - \sqrt{\frac{1}{3}} d_{5/2,-5/2} \quad (5)$$

$$e_{5/2,g} \approx \sqrt{\frac{5}{6}} d_{5/2,3/2} - \sqrt{\frac{1}{6}} d_{5/2,-5/2} \quad (6)$$

Here, Table S.II of our recent publication¹⁷ has been used to convert the natural spinor expressions from Cartesian basis to the atomic $j-j$ spinor basis, which is labeled by l_{j,m_j} . Usually, the natural spinors have definite electron occupation and carry no energetic information. However, in the present special case when there is only one occupation disincidence (the different spinors) between two states, the energy difference can be associated with the energy difference between the spinors that contain the electron. Equations 4–6 clearly explain the energy order of the two $G_{3/2,g}$ and $E_{5/2,g}$ levels. The $g_{3/2,g}$ spinors are mixtures of $3/5$ $d_{3/2}$ and $2/5$ $d_{5/2}$, while the $E_{5/2,g}$ state contains only $d_{5/2}$. Since the $d_{3/2}$ ($d_{5/2}$) spinors are stabilized (destabilized) by the SO interaction, one expects the $g_{3/2,g}$ spinor to have a lower energy than the $e_{5/2,g}$. With the atomic approximation that $d_{3/2}$ and $d_{5/2}$ are eigenstates of the effective one-electron SOC operator, one has

$$\begin{aligned} \langle e_{5/2,g} | \hat{h}_{\text{SO}} | e_{5/2,g} \rangle &= \langle g_{3/2,g} | \hat{h}_{\text{SO}} | g_{3/2,g} \rangle \\ &\approx \langle d_{5/2} | \hat{h}_{\text{SO}} | d_{5/2} \rangle - \left(\frac{2}{5} \langle d_{5/2} | \hat{h}_{\text{SO}} | d_{5/2} \rangle \right. \\ &\quad \left. + \frac{3}{5} \langle d_{3/2} | \hat{h}_{\text{SO}} | d_{3/2} \rangle \right) \\ &= \frac{3}{5} (\langle d_{5/2} | \hat{h}_{\text{SO}} | d_{5/2} \rangle - \langle d_{3/2} | \hat{h}_{\text{SO}} | d_{3/2} \rangle) \end{aligned} \quad (7)$$

Therefore, the $G_{3/2,g}$ – $E_{5/2,g}$ splitting should be $3/5$ of the $d_{5/2}$ – $d_{3/2}$ splitting. For comparison, we performed the SO-CASCI calculation for the W^{3+} cation with the $6s^2 5d^1$ configuration, which is close to the tungsten electron configuration in WF_6^- and found the SO splitting between the $d_{3/2}$ and $d_{5/2}$ spinors to be 7384 cm^{-1} . Three-fifths of this value is 4430 cm^{-1} , which is close to the 4037 cm^{-1} $G_{3/2,g}$ – $E_{5/2,g}$ splitting in WF_6^- . The latter splitting is 91% of the former, and this percentage quantifies the predominance of tungsten's d orbitals in the natural orbitals. It should be pointed out that the present use of natural spinor decomposition to explain energy ordering is unprecedented.

As Dyall concluded,⁶ the $e_{5/2,g}$ spinor has equal contributions from the three natural orbitals, so there should be no JT distortion for the $E_{5/2,g}$ state. The $g_{3/2,g}(\text{I})$ spinor has equal contributions from $t_{2g,xz}$ and $t_{2g,yz}$. Since the $t_{2g,xz}$ electron distribution pushes the fluorines on the x and z axes and the $t_{2g,yz}$ pushes those on the y and z axes, the equal contributions of the two orbitals lead to a twice as strong repulsion for axial compared to equatorial fluorines. Thus, one can predict that the $G_{3/2,g}(\text{I})$ state will undergo a distortion along the negative direction of the e_g mode in Figure 2a. The m_j values on the right-hand-side of eq 4 suggest that the $g_{3/2,g}(\text{I})$ spinor has projection of angular momentum along the z axis as $1/2$ (here, for convenience, we follow Zare's convention⁵⁶ to drop the angular momentum unit \hbar). Because the closed-shell doubly occupied electronic configuration for all other electrons in WF_6^- has zero angular momentum, the $G_{3/2,g}(\text{I})$ state also has $1/2$ angular momentum along the z axis (M_j), and this state correlates to an $E_{1/2,g}$ state of the D_{4h} double group. Because the state with only the Kramers degeneracy does not undergo the JT distortion,^{26,67,68} the $E_{1/2,g}$ state has an energy minimum in the opposite direction of the e_g mode in Figure 2a. Since the $t_{2g,xz}$ and $t_{2g,yz}$ orbitals correlate to the two components of the e_g orbital in the D_{4h} point group, this $E_{1/2,g}$ state can also be viewed as a SO coupled state from the 2E_g term at the elongated D_{4h} structure. The \hat{L}_z component of the SOC operator induces electron rotation among the $t_{2g,xz}$ and $t_{2g,yz}$ orbitals and results in a totally symmetric electron distribution in the D_{4h} point or double group (see Figure 4a), which quenches any further JT distortion. Therefore, the possible stable elongated D_{4h} structure for $G_{3/2,g}(\text{I})$ is a pure result of SOC.

Equation 2 indicates that the contributions of the $t_{2g,xy}$, $t_{2g,xz}$, and $t_{2g,yz}$ orbitals in the $g_{3/2,g}(\text{II})$ spinor are $2/3$, $1/6$, and $1/6$, respectively. Following the logic that the Cartesian subscript, e.g., “xy”, determines that the fluorines on those axes are electrostatically repelled by the extra orbital electron distribution, and weighting the repulsions by the respective orbital contributions, one can find that the $g_{3/2,g}(\text{II})$ spinor repels the equatorial fluorines $5/2$ times more than the axial fluorines. Therefore, the $G_{3/2,g}(\text{II})$ state prefers a compressed D_{4h} structure. Compared to the distortion caused by the ${}^2T_{2g,xy}$ state, the distortion caused by the $G_{3/2,g}(\text{II})$ state should have a smaller magnitude, because the push for the axial fluorines keeps them farther away from the x – y plane. This axial push stems from the $t_{2g,xz}$ and $t_{2g,yz}$ participation in the $g_{3/2,g}(\text{II})$ spinor, since the \hat{L}_y component of the SOC operator rotates the electron from the $t_{2g,xy}$ to the $t_{2g,yz}$ orbital, while the \hat{L}_x component rotates the electron to the $t_{2g,xz}$ orbital. These electron rotations are similar to the one depicted in Figure 4a. The mixing of α and β spins in eq 2 comes from the action of \hat{s}_x or \hat{s}_y ,¹⁴ which comes with the \hat{L}_x or \hat{L}_y induced rotation. In general, the SO effects are known to reduce the e_g mode distortion of an O_h molecule.⁶⁹ However, to the best of our knowledge, the present work is the first to present a pictorial orbital explanation for this reduction.

The relation between Cartesian and spherical tensors determines that the combination of $d_{xz} + id_{yz}$ has an angular momentum projection on the z axis of $+1$. Adding the $1/2$ spin angular momentum of α leads to total angular momentum projection of $3/2$. Thus, the $t_{2g,xz}\alpha + it_{2g,yz}\alpha$ combination in eqs 2 and 3 corresponds to $m_j = 3/2$, and both the $G_{3/2,g}(\text{II})$ and $E_{5/2,g}$ states correlate to two $E_{3/2,g}$ states in the D_{4h} double group. The composition of eq 2 also indicates that the lower energy $E_{3/2,g}$ state at the compressed D_{4h} structure mainly ($2/3$) stems from the ${}^2B_{2g}$ (“xy”) state, with some ($1/3$) SOC mixing of the 2E_g (“xz” and “yz”) state.

We now consider the t_{2g} distortions leading to D_{3d} structures. Using the basis functions ψ_1 , ψ_2 , and ψ_3 , the natural spinors are calculated to be

$$g'_{3/2,g}(\text{I}) = \sqrt{\frac{1}{2}}\psi_2\beta + i\sqrt{\frac{1}{2}}\psi_3\beta \quad (8)$$

$$g'_{3/2,g}(\text{II}) = \sqrt{\frac{2}{3}}\psi_1\beta - \left(\sqrt{\frac{1}{24}} + i\sqrt{\frac{1}{8}}\right)\psi_2\alpha + \left(\sqrt{\frac{1}{8}} - i\sqrt{\frac{1}{24}}\right)\psi_3\alpha \quad (9)$$

$$e'_{5/2,g} = \left(\frac{1}{2} + i\sqrt{\frac{1}{12}}\right)\psi_1\beta + i\sqrt{\frac{1}{3}}\psi_2\alpha - \sqrt{\frac{1}{3}}\psi_3\alpha \quad (10)$$

A prime is used to distinguish these spinors and electronic states from those having the same symbols but in the basis of the $t_{2g,xyy}$, $t_{2g,xzz}$, and $t_{2g,yyz}$ orbitals (eqs 1–3). Neglecting fluorine contributions, those spinors can be expressed in terms of the Cartesian 5d orbitals of tungsten as

$$g'_{3/2,g}(\text{I}) \approx \left(\frac{1}{4} - i\frac{\sqrt{3}}{4}\right)d_{xx}\beta - \left(\frac{1}{4} - i\frac{\sqrt{3}}{4}\right)d_{yy}\beta + \left(\frac{1}{2} + i\sqrt{\frac{1}{12}}\right)d_{xy}\beta - \left(\sqrt{\frac{1}{24}} - i\sqrt{\frac{1}{8}}\right)d_{xz}\beta + \left(\sqrt{\frac{1}{8}} + i\sqrt{\frac{1}{24}}\right)d_{yz}\beta \quad (11)$$

$$g'_{3/2,g}(\text{II}) \approx -\sqrt{\frac{1}{12}}d_{xx}\alpha + \sqrt{\frac{1}{12}}d_{yy}\alpha - \frac{i}{3}d_{xy}\alpha + \sqrt{\frac{1}{18}}d_{xz}\alpha - i\sqrt{\frac{1}{18}}d_{yz}\alpha - \sqrt{\frac{1}{6}}d_{xx}\beta - \sqrt{\frac{1}{6}}d_{yy}\beta + \sqrt{\frac{2}{3}}d_{zz}\beta \quad (12)$$

$$e'_{5/2,g} \approx -\left(\sqrt{\frac{1}{8}} + i\sqrt{\frac{1}{24}}\right)d_{xx}\alpha + \left(\sqrt{\frac{1}{8}} + i\sqrt{\frac{1}{24}}\right)d_{yy}\alpha + \left(\sqrt{\frac{1}{18}} - i\sqrt{\frac{1}{6}}\right)d_{xy}\alpha + \left(\sqrt{\frac{1}{12}} + \frac{i}{6}\right)d_{xz}\alpha + \left(\frac{1}{6} - i\sqrt{\frac{1}{12}}\right)d_{yz}\alpha + \left(\frac{1}{4} + i\sqrt{\frac{1}{48}}\right)d_{xx}\beta + \left(\frac{1}{4} + i\sqrt{\frac{1}{48}}\right)d_{yy}\beta + i\sqrt{\frac{1}{12}}d_{zz}\beta \quad (13)$$

These expressions are obtained by extracting the coefficients of the tungsten d basis functions in the spinors and renormalizing them. Since equally averaging the ${}^2A_{1g}$ (with the extra electron occupying ψ_1) and the two components of 2E_g (the extra electron in ψ_2 or ψ_3) produces a totally symmetric electron distribution and quenches the JT distortion, we can judge that the “bend-down” force created by ψ_1 is balanced by the total “bend-up” force exerted by both ψ_2 and ψ_3 . The $e'_{5/2,g}$ spinor contains equal contributions from the three natural orbitals, and this quenches the D_{3d} distortion, just as was the case for the $e_{5/2,g}$ spinor for D_{4h} distortion. The $d_{xz}\alpha - id_{yz}\alpha$ combination ($m_j = 1/2$) in eq 13 indicates that this state correlates to the $E_{1/2,g}$ state in the D_{3d} double group.

The $G'_{3/2,g}(\text{I})$ state prefers an elongated D_{3d} structure (the structure results from the opposite distortion of Figure 2b) since it has pure contributions from ψ_2 and ψ_3 . This state stems from the action of the $\hat{l}_z\hat{s}_z$ component of the SOC operator, and it also has a totally symmetric electron distribution in the D_{3d} point group (see Figure 4b). Therefore, the elongated D_{3d} structure can be stabilized as a pure result of the SO effect. The $d_{xz}\beta - id_{yz}\beta$ combination in eq 11 has $m_j = -3/2$, and the $G'_{3/2,g}(\text{I})$ state correlates to an $E_{3/2,g}$ state in the D_{3d} double group. The pure contribution from the ψ_2 and ψ_3 in eq 8 also indicates that this $E_{3/2,g}$ state can be viewed as the SO coupled state from the 2E_g state at the elongated D_{3d} structure. The $g'_{3/2,g}(\text{II})$ has 2 times greater contribution from ψ_1 than the sum of ψ_2 and ψ_3 , so the $G'_{3/2,g}(\text{II})$ state favors a compressed D_{3d} structure. Also, similarly to the case of the $G_{3/2,g}(\text{II})$ state, the participation of ψ_2 and ψ_3 reduces the magnitude of the distortion. Their participation is the result of the $\hat{l}_x\hat{s}_x$ and $\hat{l}_y\hat{s}_y$ induced electron rotation from ψ_1 to ψ_2 and ψ_3 , which are mainly composed of $d_{x^2-y^2}$, d_{xy} , d_{xz} , and d_{yz} (the first four terms on the right-hand side of eq 12). These d components stem from their nonzero matrix elements of \hat{l}_x or \hat{l}_y operators with the $d_{2z^2-x^2-y^2}$ (the last three terms on the right-hand side of eq 12). The associated spin-flipping is also observed in eq 12. The $\hat{l}_x\hat{s}_x$ induced rotations are depicted in Figure 4c and d, and the $\hat{l}_y\hat{s}_y$ analogues are similar. The $d_{xz}\alpha - id_{yz}\alpha$ combination in eq 12 has $m_j = -1/2$, and the $G'_{3/2,g}(\text{II})$ state correlates to an $E_{1/2,g}$ state in the D_{3d} double group. The coefficients in eq 9 suggest that this $E_{1/2,g}$ state stems mainly (2/3) from the ${}^2A_{1g}$ state (ψ_1), with some (1/3) SOC mixing of the 2E_g state (ψ_2 and ψ_3) at the D_{3d} structure. Since the $E_{5/2,g}$ state at the O_h structure does not lead to distortion along either mode in Figure 2, we will omit this state in the following discussion, and the PES of such a state, with a minimum at the O_h structure, will not be presented in the next subsection.

The natural spinor analysis indicates that the $G_{3/2,g}$ state undergoes similar e_g and t_{2g} distortions as the spin-free ${}^2T_{2g}$ state, and this is consistent with the O_h double group anti-symmetric direct product decomposition of $\{G_{3/2,g} \otimes G_{3/2,g}\} = A_{1g} \oplus E_g \oplus T_{2g}$.²⁶ (Note that for the SOC electronic states, it is their irreps' anti-symmetric direct product that determines the symmetry of the JT active modes.^{67,68}) However, one should notice that the SO effect leads to energy minima at the elongated D_{4h} and D_{3d} structures, which are absent in the spin-free cases. It is interesting to compare the complete SOC quenching of JT for WF_5 ²⁴ and the present incomplete quenching (only the $E_{5/2,g}$ component of the ${}^2T_{2g}$ retains high symmetry) for WF_6^- . Although both cases contain odd numbers of electrons and have Fermion irreps¹⁴ of their respective double groups, the D_{3h} double group of WF_5 has only two-dimensional Fermion irreps ($E_{1/2,3/2,5/2}$) that represent only the time-reversal degeneracy, not the spatial degeneracy that the JT effect can remove.^{26,67} On the contrary, the O_h double group of WF_6^- has four-dimensional Fermion irreps ($G_{3/2,(g,u)}$) that contain both time-reversal and spatial degeneracies. It is the spatial degeneracy in the n -fold ($n > 2$) Fermion irreps that triggers the JT distortion. In the following subsection, we investigate the PES of the states deriving from the ${}^2T_{2g}$ and $G_{3/2,g}$ states to verify the predictions based on the natural orbital and natural spinor analyses.

Potential Energy Surfaces along the Distortions and the Natural Spinor Analysis. Figure 2a indicates that the PES along the e_g distortion depends on two variables: the W–F bond length along the z axis (r_z) and the one along the x or y axis (r_x, r_y) in the coordinate system of Figure 1a. The D_{4h} geometry is called compressed when $r_z < r_x$ or elongated if $r_z > r_x$. The symmetry is

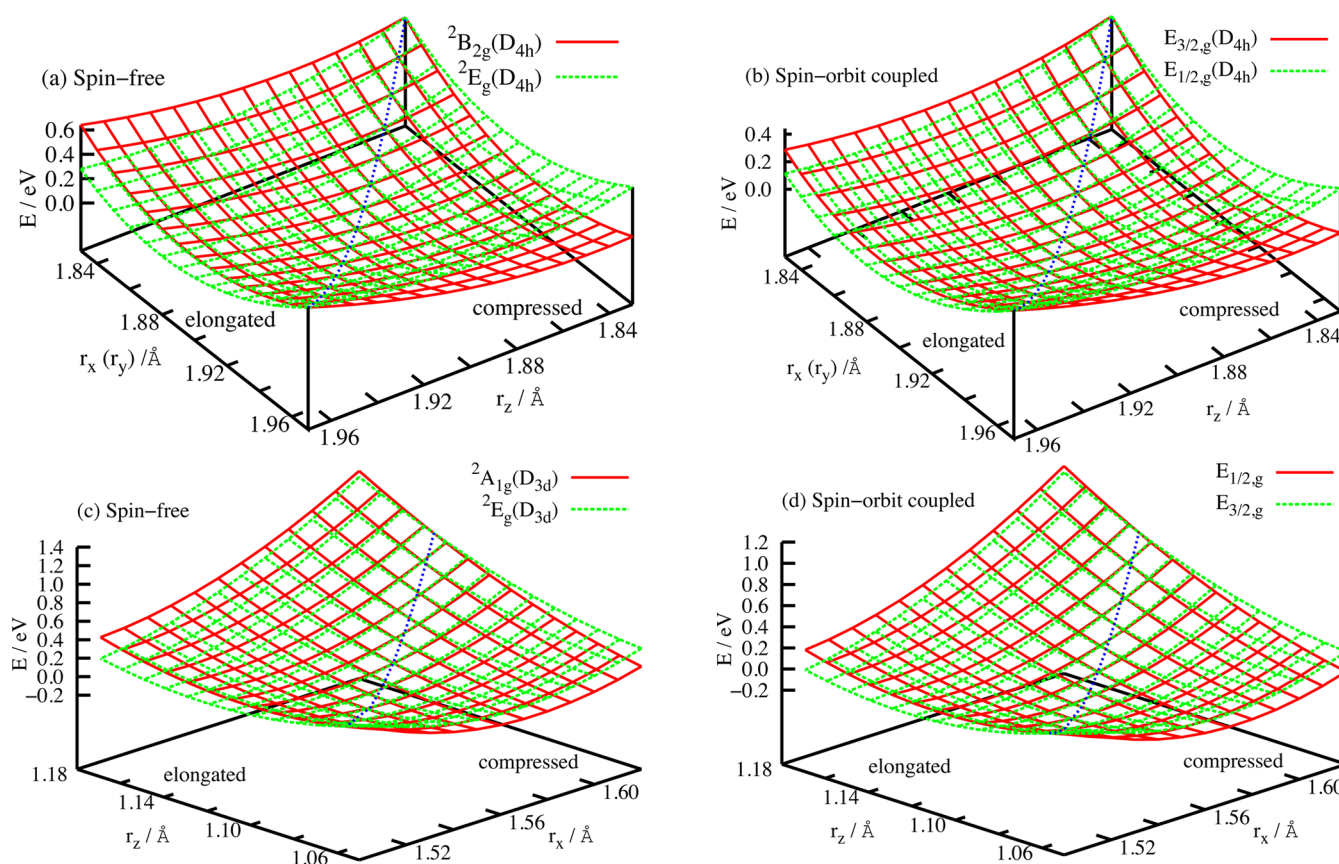


Figure 5. CASCI potential energy surfaces of the states derived from the ${}^2T_{2g}$ and $G_{3/2g}$ states at the O_h structure under the e_g (D_{4h}) and t_{2g} (D_{3d}) distortions: (a) spin-free states under the e_g distortion, (b) spin-orbit coupled states under the e_g distortion, (c) spin-free states under the t_{2g} distortion, (d) spin-orbit coupled states under the t_{2g} distortion. The blue dotted curves represent the crossing seams of the PESs, corresponding to the O_h structure of WF_6^- . One should notice the different meanings of r_x and r_z under different distortions.

Table 1. Structural Parameters and the Jahn–Teller Stabilization Energies (E_{JT}) of the PES Minima in WF_6^-

e_g distortion					t_g distortion			
	state (D_{4h}) ^a	r_z (Δr_z) ^b /Å	r_x (Δr_x) ^b /Å	E_{JT} ^c /eV	state (D_{3d}) ^a	r_{WF} (Δr_{WF}) ^{b,d} /Å	θ ($\Delta\theta$) ^{b,d} /deg	E_{JT} ^c /eV
CI ^e	${}^2B_{2g}$	1.858 (−0.034)	1.910 (0.018)	0.049	${}^2A_{1g}$	1.893 (0.001)	33.7 (−1.6)	0.050
	${}^2E_g^f$	1.909 (0.017)	1.884 (−0.008)	0.011	${}^2E_g^f$	1.886 (−0.006)	36.2 (0.9)	0.007
	$E_{3/2g}$	1.872 (−0.020)	1.903 (0.011)	0.014	$E_{1/2g}$	1.889 (−0.003)	34.1 (−1.2)	0.025
	$E_{1/2g}$	1.909 (0.017)	1.884 (−0.008)	0.011	$E_{3/2g}$	1.886 (−0.006)	36.2 (0.9)	0.016
	${}^2B_{2g}$	1.868 (−0.041)	1.932 (0.023)	0.064	${}^2A_{1g}$	1.913 (0.004)	33.4 (−1.9)	0.057
PT ^e	${}^2E_g^f$	1.930 (0.021)	1.900 (−0.009)	0.015	${}^2E_g^f$	1.910 (0.001)	36.2 (0.9)	0.013
	$E_{3/2g}$	1.884 (−0.025)	1.923 (0.014)	0.020	$E_{1/2g}$	1.910 (0.001)	33.7 (−1.6)	0.030
	$E_{1/2g}$	1.930 (0.021)	1.900 (−0.009)	0.015	$E_{3/2g}$	1.910 (0.001)	36.5 (1.2)	0.023

^aThe state symbols are labeled using the point or double group to which the distortion belongs. ^bThe Δr_z values (etc.) indicate the magnitude of the distortion, and they are calculated by subtracting the parameters of the undistorted structure (see text) from the distorted ones. ^cFor the spin-free states, the values of E_{JT} are calculated as the energy lowering from the ${}^2T_{2g}$ state at the predistorted structure. For the spin-orbit coupled states, the E_{JT} values represent the lowering from the $G_{3/2g}$ state. ^dThe parameters (r_x and r_z) of the D_{3d} structure have been converted to the natural parameters, W–F bond length (r_{WF}) and the angle (θ) between the bond and the reflection plane of the \hat{S}_6 improper rotation. ^eFor the spin-free (spin-orbit coupled) state, CI means CASCI (SO-CASCI) and similarly for PT. ^fAs discussed in the text, the 2E_g states are not stable and will undergo further JT distortions. Their values are listed here only for comparison.

O_h when ($r_x = r_y$) = r_z . For the PES along the t_{2g} distortion, the natural variables are the W–F bond length (r_{WF}) and the angle (θ) between the W–F bond and the reflection plane of the S_6 improper rotation. In terms of the input files for calculations, these can be transformed into the ($r_x, 0, r_z$) coordinates of a unique F atom in a σ_d plane of D_{3d} in the coordinate system of Figure 1d, by $r_{WF} = (r_x^2 + r_z^2)^{1/2}$ and $\theta = \arctan(r_z/r_x)$. O_h geometry occurs when $r_x = \sqrt{2}r_z$, i.e., $\theta = 35.3^\circ$. The D_{3d}

geometry is called compressed if $\sqrt{2}r_z < r_x$ or elongated if the reverse is true. Note that r_x and r_z have different meanings for D_{4h} and D_{3d} . The total energies were calculated on grids that were scanned with a spacing of 0.02 Å and refined around minima with a spacing of 0.001 Å.

The CASCI and SO-CASCI PESs are illustrated in Figure 5. The corresponding MCQDPT and SO-MCQDPT PES are qualitatively the same, and they are not shown. The structural

parameters and JT stabilization energies of the distorted geometries are listed in Table 1. In the discussion below, we use a symbol like ${}^2E_g(D_{4h})$ to specify which group the irrep belongs to, as the D_{4h} and D_{3d} point and double groups share the same symbols for some irreps.

Figure 5a,b present the spin-free and SO coupled PESs along the e_g distortion, and they are in perfect agreement with the predictions from the natural orbitals and natural spinors, as given in the preceding subsection. The two spin-free sheets cross at the O_h structure (the diagonal seam of $r_z = r_x$) and the ${}^2B_{2g}(D_{4h})$ and $E_{3/2,g}(D_{4h})$ sheets are lower at the $r_z < r_x$ (compressed) region while the $E_g(D_{4h})$ and $E_{1/2,g}(D_{4h})$ prefer the opposite region.

The t_{2g} distortion into D_{3d} is shown in Figure 5c,d. The ${}^2A_{1g}(D_{3d})$ and $E_{1/2,g}(D_{3d})$ sheets are lower at the large r_x and small r_z (compressed) regions while the ${}^2E_g(D_{3d})$ and $E_{3/2,g}(D_{3d})$ prefer the opposite. All of the PESs are consistent with the predictions from the natural orbitals and natural spinors. The ratios between Δr_z and Δr_x for each D_{4h} minimum in Table 1 are all close to -2 , which is the ideal ratio between the r_z and r_x displacements in the e_g normal mode.²⁶ The Δr_{WF} for all of the D_{3d} minima are almost zero, and this means the distortion is of pure angular nature, being consistent with the ideal t_{2g} normal mode.²⁶ The distortion magnitudes are generally small, as the largest absolute Δr in the e_g distortion is 0.023 Å and the largest absolute $\Delta\theta$ in the t_{2g} distortion is 1.9°. The values of E_{JT} are also small, with the largest one being only 0.064 eV. We attribute the small distortion magnitudes and E_{JT} to the compact distribution of the extra electron, due to the highly electron-deficient character of the tungsten center. With the limited spatial extension, the nontotally symmetric electrostatic repulsion between the extra electron and the fluorines would be largely quenched by the totally symmetric attraction between tungsten and fluorine, leading to only minute distortions.

For both the ${}^2B_{2g}(D_{4h})$ and ${}^2A_{1g}(D_{3d})$ states, the inclusion of the SO effect reduces the distortion magnitudes, as predicted by the natural spinors. For instance, at the CI level, the distortion magnitude ($\Delta r_z, \Delta r_x$) is reduced from $(-0.034 \text{ Å}, 0.018 \text{ Å})$ of the ${}^2B_{2g}(D_{4h})$ to $(-0.020 \text{ Å}, 0.011 \text{ Å})$ of the $E_{3/2,g}(D_{4h})$ state, and the $\Delta\theta$ is reduced from -1.6° of the ${}^2A_{1g}(D_{3d})$ to -1.2° of the $E_{1/2,g}(D_{3d})$ state. Along with the distortion magnitudes, their E_{JT} values are also reduced, from 0.049 to 0.014 eV for the ${}^2B_{2g}(D_{4h})$ state in the e_g distortion and from 0.050 to 0.025 eV for the ${}^2A_{1g}(D_{3d})$ state in the t_{2g} distortion. This is because at the compressed D_{4h} (D_{3d}) structure, the b_{2g} (a_{1g}) orbital, which stems from the $t_{2g,xy}$ (ψ_1) at the O_h structure, has a lower energy than the e_g (e_g) degenerate set that stems from the $t_{2g,xz}$ and $t_{2g,yz}$ (ψ_2 and ψ_3). Consequently, the electron rotation from the b_{2g} (a_{1g}) to the e_g (e_g) set is hindered, unlike the free rotation among the t_{2g} set (ψ_1, ψ_2 , and ψ_3) at the O_h structure. Thus, the SO effect reduces the energy more at the O_h than at the compressed D_{4h} and D_{3d} structures, resulting in a smaller value of E_{JT} for the SO coupled states at the two structures. This rationalization is further corroborated by the natural spinor analysis. The natural spinor for the $E_{3/2,g}(D_{4h})$ state at its CI-compressed D_{4h} structure in Table 1 is calculated to be

$$e_{3/2,g} = 0.859067b_{2g,xy}\beta + i0.361942e_{g,xz}\alpha - 0.361942e_{g,yz}\alpha \quad (14)$$

where the subscripts "xy" etc. correspond to the t_{2g} set in Figure 1. Compared to eq 2, one sees there is a decrease of contributions from the d_{xz} and d_{yz} orbitals, as the result of the aforementioned hindered rotation. Extracting only the tungsten 5d orbitals in such a spinor and renormalizing it, we obtain

$$\begin{aligned} e_{3/2,g} &\approx 0.858765d_{xy}\beta + i0.362300d_{xz}\alpha - 0.362300d_{yz}\alpha \\ &= 0.772269d_{3/2,3/2} - 0.607238d_{5/2,-5/2} \\ &\quad - 0.186713d_{5/2,3/2} \end{aligned} \quad (15)$$

where the same procedure in obtaining eqs 4–6 has been used, and this expression gives 0.5964 $d_{3/2}$ and 0.4036 $d_{5/2}$ contributions. The decrease of $d_{3/2}$ and increase of $d_{5/2}$ contributions reflect the reduced SOC stabilization. The natural spinor of the $E_{1/2,g}(D_{3d})$ state at the compressed D_{3d} structure is calculated to be

$$\begin{aligned} e_{1/2,g} &= 0.857088a_{1g,\psi_1}\beta - (0.182140 + i0.315476)e_{g,\psi_2}\alpha \\ &\quad + (0.315476 - i0.182140)e_{g,\psi_3}\alpha \end{aligned} \quad (16)$$

and the similar reduction of the ψ_2 and ψ_3 contribution due to the hindered rotation is obvious when compared with eq 9. On the other hand, in the D_{3d} point group, s orbitals at the tungsten center are of the A_{1g} irrep as we do observe non-negligible s contributions in the a_{1g} orbital. The decrease of the total d components also contributes to the reduction of SOC stabilization.

It is interesting to observe in Table 1 that the ${}^2E_g(D_{4h})$ and $E_{1/2,g}(D_{4h})$ states have identical e_g distortion magnitudes and E_{JT} at both CI and PT correlation levels; i.e., the SO effect appears to have no influence on the distortion. Along the change from the O_h to the elongated D_{4h} structure, the two components of the ${}^2E_g(D_{4h})$ state have to be averaged with equal weights in energy calculation to maintain their degeneracy. Therefore, the elongated D_{4h} structure in Table 1 is the result of an action by the average of both components. As the discussion about eq 1 in the last subsection indicates, in the $E_{1/2,g}(D_{4h})$ state, the structure is also distorted by the action of the same two components, leading to the identical elongated D_{4h} structure as in the spin-free case. The identical E_{JT} values suggest that the SOC stabilizations are identical at both the O_h and elongated D_{4h} structures. This is because the $e_{g,xz}$ and $e_{g,yz}$ orbitals remain degenerate along the distortion, and the SOC induced rotation among those two orbitals remains unhindered as for the O_h structure, giving the natural spinor:

$$e_{1/2,g} = \sqrt{\frac{1}{2}}e_{g,xz}\beta + i\sqrt{\frac{1}{2}}e_{g,yz}\beta \quad (17)$$

which is identical to the $g_{3/2,g}(I)$ spinor (eq 1) and can also be decomposed to the same $d_{3/2}/d_{5/2}$ ratio (3:2).

More interestingly, the inclusion of the SO effect enhances the distortion for the ${}^2E_g(D_{3d})$ state along the t_g mode. Both the CI and PT E_{JT} of the $E_{3/2,g}(D_{3d})$ state are about twice those of the ${}^2E_g(D_{3d})$ state, and the PT $\Delta\theta$ increases from 0.9° to 1.2°. This suggests that the SOC stabilization is even larger at the elongated D_{3d} structure. We obtain the natural spinor for the $E_{3/2,g}(D_{3d})$ state as

$$e_{3/2,g} = \sqrt{\frac{1}{2}}e_{g,\psi_2}\beta + i\sqrt{\frac{1}{2}}e_{g,\psi_3}\beta \quad (18)$$

which is associated with the $g'_{3/2,g}(I)$ spinor (eq 8); however, this spinor is decomposed to 0.6116 $d_{3/2}$ and 0.3883 $d_{5/2}$ contributions. The gain of $d_{3/2}$ and loss of $d_{5/2}$ components compared to the $g'_{3/2,g}(I)$ spinor explains the greater SOC stabilization at the elongated D_{3d} structure. It seems puzzling that the $e_{3/2,g}$ spinor in the D_{3d} double group (eq 18) has the same

formula as the $e_{1/2,g}$ spinor in the D_{4h} double group (eq 17) while they have different $d_{3/2}$ and $d_{5/2}$ contributions. The answer lies in the higher-lying orbitals with d components. The two virtual orbitals with significant d character are plotted in Figure 1g–h. These two orbitals can be easily associated with $d_{z^2-x^2-y^2}$ and $d_{x^2-y^2}$ in the O_h or D_{4h} symmetry. Because they are of the A_{1g} and B_{1g} irreps of the D_{4g} point group, they are not mixed with the $e_{g,xz}$ and $e_{g,yz}$ orbitals along the e_g distortion. Therefore, the d components in the $t_{2g,xz}$ and $t_{2g,yz}$ orbitals are preserved and so are the $d_{3/2}$ and $d_{5/2}$ contributions. However, the two virtual orbitals are of the E_g irrep in the D_{3d} point group, and they can be mixed with the original ψ_2 and ψ_3 along the t_{2g} distortion. This mixing can change both the d components in the e_{g,ψ_2} and e_{g,ψ_3} orbitals as well as the $d_{3/2}$ and $d_{5/2}$ contributions. Our natural spinor analysis indicates that this mixing leads to a gain (loss) of the $d_{3/2}$ ($d_{5/2}$) character and, consequently, to an increased SOC stabilization. A SOC enhancement of the JT distortion is seldom reported in the literature, but this occurs in the present ${}^2E_g(D_{3d})$ case, and the natural spinors provide a clear explanation for this phenomenon.

The SO-MCQDPT values of E_{JT} (as well as SO-CASCI) in Table 1 indicate that the compressed D_{3d} structure (with $E_{JT} = 0.030$ eV) is the most stable configuration, and thus the ground state of WF_6^- is predicted to be an $E_{1/2,g}(D_{3d})$ state. However, the other minima only have slightly higher energies, maximally 0.015 eV, so they can be easily reached by thermal population, unless at very low temperature. On the other hand, the fundamental harmonic vibrational frequencies for the e_g and t_{2g} normal modes of the neutral WF_6 molecule, calculated using the MP2 method, are 615.96 cm^{-1} and 306.70 cm^{-1} , corresponding to the energy quanta $\hbar\omega$ of 0.076 and 0.038 eV. Although for the WF_6^- anion the frequencies are expected to be somewhat lower because of its looser structure, we believe the vibrational energy quanta of the two modes are comparable to the small E_{JT} , and a “weak vibronic coupling” solution²⁶ for this system is expected.

CONCLUSIONS

The potential energy surfaces of the WF_6^- anion under different symmetries have been studied, focusing on the Jahn–Teller distortion of this species and its interplay with the spin–orbit effect. By performing the spin–orbit coupling calculations we have found that at octahedral geometry the ground state of WF_6^- is a quadruply degenerate $G_{3/2,g}$ state, which can undergo the Jahn–Teller distortions along either e_g or t_{2g} vibrational modes. The t_{2g} distortion omitted in the previous study⁶ has been investigated, and the global minimum of the ground state potential energy surface was found to be located along this distortion. The inclusion of the spin–orbit effect tends to enhance the t_{2g} distortion along its reverse direction when the system is in the 2E_g state. This result is a rare example of the SOC enhancement of the Jahn–Teller distortion, and it stands in contrast to the previously predicted complete SOC quenching of the distortion in WF_6 .^{6,24} The energies of the other minima along the two distortions are slightly higher, and they can be thermally populated. The comparison between the Jahn–Teller stabilization energies and the typical vibrational energy quanta suggests a “weak vibronic coupling” for this system.

The natural spinor analysis was shown to be very useful for the understanding of the described phenomena. The topology of the natural spinors sheds light on the possible Jahn–Teller distortion modes for a spin–orbit coupled state and the interplay (both quenching and enhancing) between spin–orbit and Jahn–Teller effects. The decomposition of the natural spinors into atomic

spinors clearly explains the observed energy ordering for the SOC states. On the basis of the computed decomposition of the spinors into molecular (and atomic) orbitals and the electrostatic repulsion in this ionic compound, we can predict the energies and the consequent geometry distortions for various symmetries. Despite its simple mathematical formulation, the concept of natural spinors allows us to probe deeply in relativistic quantum chemistry. We hope that the present case study may promote the use of this concept in the future.

AUTHOR INFORMATION

Corresponding Author

*E-mail: mariusz.klobukowski@ualberta.ca.

Present Address

^{||}Department of Chemistry, University of Waterloo, Waterloo, Ontario, Canada, N2L 3G1

Notes

The authors declare no competing financial interest.

ACKNOWLEDGMENTS

T.Z. expresses his gratitude to the Alberta Ingenuity Funds, Killam Trusts, and Alberta Scholarship Program for the graduate student scholarships. M.K. thanks the Natural Sciences and Engineering Research Council of Canada for the support of the present project under Research Grant No. G121210414. M.W.S. acknowledges support by the DOE Chemical Physics program. The calculations were performed on the Linux clusters at the Department of Chemistry and Department of Academic Information and Communication Technologies at the University of Alberta. We are grateful to Professor M. S. Gordon for his continuing support of the development of the GAMESS-US program suite.

REFERENCES

- (1) Lassner, E.; Schubert, W.-D. *Tungsten: properties, chemistry, technology of the element, alloys and chemical compounds*; Springer-Verlag: Germany, 1999.
- (2) Yu, M. L.; Ahn, K. Y.; Joshi, R. V. *IBM J. Res. Dev.* **1990**, *34*, 875–883.
- (3) Madar, R.; Bernard, C. J. *Vac. Sci. Technol. A* **1990**, *8*, 1413–1421.
- (4) Arora, R.; Pollard, R. J. *Electrochem. Soc.* **1991**, *138*, 1523–1537.
- (5) Kuijlaars, K. J.; Kleijn, C. R.; van den Akker, H. E. A. *Thin Solid Films* **1995**, *270*, 456–461.
- (6) Dyal, K. G. *J. Phys. Chem. A* **2000**, *104*, 4077–4083.
- (7) Chen, H.; Andersson, P.; Lindahl, A. O.; Hanstorp, D. *Chem. Phys. Lett.* **2011**, *511*, 196–200.
- (8) Fedorov, D. G.; Koseki, S.; Schmidt, M. W.; Gordon, M. S. *Int. Rev. Phys. Chem.* **2003**, *22*, 551–592.
- (9) Marian, C. M. In *Fine and Hyperfine Structure: Spin Properties of Molecules*; Wilson, S., Diercksen, G. H. F., Eds.; Kluwer Academic Publishers: Dordrecht, The Netherlands, 1997; pp 291–351.
- (10) David, J.; Guerra, D.; Restrepo, A. *Inorg. Chem.* **2011**, *50*, 1480–1483.
- (11) Pérez-Villa, A.; David, J.; Fuentealba, P.; Restrepo, A. *Chem. Phys. Lett.* **2011**, *507*, 57–62.
- (12) Fedorov, D. G. Ph.D. thesis, Iowa State University, Ames, IA, 1999.
- (13) Fedorov, D. G.; Gordon, M. S. Symmetry in spin-orbit coupling. *Low-Lying Potential Energy Surfaces*; American Chemical Society: Washington, DC, 2002.
- (14) Marian, C. M. In *Spin-Orbit Coupling in Molecules*; Lipkowitz, K. B., Boyd, D. B., Eds.; Wiley-VCH: New York, 2001; Vol. 17, pp 99–204.
- (15) Alekseyev, A. B.; Liebermann, H.-P.; Buenker, R. J. In *Spin-Orbit Multireference Configuration Interaction Method and Applications to*

Systems Containing Heavy Atoms; Hirao, K., Ishikawa, Y., Eds.; World Scientific: Singapore, 2004; pp 65–105.

(16) Fedorov, D. G.; Schmidt, M. W.; Koseki, S.; Gordon, M. S. In *Spin-Orbit Coupling Methods and Applications to Chemistry*; Hirao, K., Ishikawa, Y., Eds.; World Scientific: Singapore, 2004; pp 107–136.

(17) Zeng, T.; Fedorov, D. G.; Schmidt, M. W.; Klobukowski, M. J. *Chem. Phys.* **2011**, *134*, 214108.

(18) Vallet, V.; Maron, L.; Teichteil, C.; Flament, J.-P. *J. Chem. Phys.* **2000**, *113*, 1391–1402.

(19) Das, K. K.; Petsalakis, I. D.; Liebermann, H.-P.; Alekseyev, A. B. *J. Chem. Phys.* **2002**, *116*, 608–616.

(20) Barandiarán, Z.; Seijo, L. *J. Chem. Phys.* **2003**, *118*, 7439–7456.

(21) Sánchez-Sanz, G.; Barandiarán, Z.; Seijo, L. *Chem. Phys. Lett.* **2010**, *498*, 226–228.

(22) Danilo, C.; Vallet, V.; Flament, J.-P.; Wahlgren, U. *J. Chem. Phys.* **2008**, *128*, 154310.

(23) Brozell, S. R.; Shepard, R. J. *Phys. Chem. A* **2009**, *113*, 12741–12747.

(24) Zeng, T.; Fedorov, D. G.; Schmidt, M. W.; Klobukowski, M. J. *Chem. Theory Comput.* **2011**, *7*, 2864–2875.

(25) Barckholtz, T. A.; Miller, T. A. *Int. Rev. Phys. Chem.* **1998**, *17*, 435–524.

(26) Bersuker, I. B. *The Jahn-Teller Effect*; Cambridge University Press: Cambridge, U.K., 2006.

(27) *The Jahn-Teller Effect and Beyond*; Boggs, J. E., Polinger, V. Z., Eds.; The Academy of Sciences of Moldova and The University of Texas at Austin: Austin, TX, 2008.

(28) George, P. M.; Beauchamp, J. L. *Chem. Phys.* **1979**, *36*, 345–351.

(29) Viggiano, A. A.; Paulson, J. F.; Dale, F.; Henchman, M.; Adams, N. G.; Smith, D. J. *Phys. Chem.* **1985**, *89*, 2264–2267.

(30) Dispert, H.; Lacmann, K. *Chem. Phys. Lett.* **1977**, *45*, 311–315.

(31) Reents, W. D., Jr.; Mandich, M. L.; Bondybey, V. E. *Chem. Phys. Lett.* **1986**, *131*, 1–7.

(32) Mazej, Z.; Hagiwara, R. *J. Fluorine Chem.* **2007**, *128*, 423–437.

(33) Burgess, J.; Peacock, R. D. *J. Fluorine Chem.* **1977**, *10*, 479–486.

(34) Poluyanov, L. V.; Domcke, W. *Spin-Orbit Vibronic Coupling in Jahn-Teller and Renner Systems. Jahn-Teller Effect: Fundamentals and Implications for Physics and Chemistry*; Springer: New York, **2009**; pp 77–97.

(35) Opalka, D.; Segado, M.; Poluyanov, L. V.; Domcke, W. *Phys. Rev. A* **2010**, *81*, 042501.

(36) Mondal, P.; Opalka, D.; Poluyanov, L. V.; Domcke, W. *Chem. Phys.* **2011**, *387*, 56–65.

(37) Mondal, P.; Opalka, D.; Poluyanov, L. V.; Domcke, W. *J. Chem. Phys.* **2012**, *136*, 084308.

(38) Opalka, D.; Poluyanov, L. V.; Domcke, W. *J. Chem. Phys.* **2011**, *135*, 104108.

(39) Poluyanov, L. V.; Domcke, W. *Chem. Phys.* **2010**, *374*, 86–93.

(40) Alvarez-Thon, L.; David, J.; Arratia-Pérez, R.; Seppelt, K. *Phys. Rev. A* **2008**, *77*, 034502.

(41) Stevens, W. J.; Basch, H.; Krauss, M. *J. Chem. Phys.* **1984**, *81*, 6026–6033.

(42) Stevens, W. J.; Krauss, M.; Basch, H.; Jasien, P. G. *Can. J. Chem.* **1992**, *70*, 612–630.

(43) Cundari, T. R.; Stevens, W. J. *J. Chem. Phys.* **1993**, *98*, 5555–5565.

(44) Wood, J. H.; Boring, A. M. *Phys. Rev. B* **1978**, *18*, 2701–2711.

(45) Hay, P. J.; Wadt, W. R. *J. Chem. Phys.* **1985**, *82*, 270–283.

(46) Dunning, T. H. *J. Chem. Phys.* **1989**, *90*, 1007–1023.

(47) Davidson, E. R.; Jarzecki, A. A. In *Multi-Reference Perturbation Theory*; Hirao, K., Ed.; World Scientific: Singapore, 1999; pp 31–64.

(48) Nakano, H. *J. Chem. Phys.* **1993**, *99*, 7983–7992.

(49) Nakano, H. *Chem. Phys. Lett.* **1993**, *207*, 372–378.

(50) Fedorov, D. G.; Gordon, M. S. *J. Chem. Phys.* **2000**, *112*, 5611–5623.

(51) Fedorov, D. G.; Finley, J. P. *Phys. Rev. A* **2001**, *64*, 042502.

(52) Koseki, S.; Schmidt, M. W.; Gordon, M. S. *J. Phys. Chem. A* **1998**, *102*, 10430–10435.

(53) Choe, Y.-K.; Witek, H. A.; Finley, J. P.; Hirao, K. *J. Chem. Phys.* **2001**, *114*, 3913–3918.

(54) Witek, H. A.; Choe, Y.-K.; Finley, J. P.; Hirao, K. *J. Comput. Chem.* **2002**, *23*, 957–965.

(55) Stowasser, R.; Hoffmann, R. *J. Am. Chem. Soc.* **1999**, *121*, 3414–3420.

(56) Zare, R. N. *Angular Momentum: Understanding Spatial Aspects in Chemistry and Physics*; John Wiley and Sons, Inc.: New York, 1988.

(57) Zeng, T. Ph.D. thesis, University of Alberta, Edmonton, Alberta, Canada, 2010.

(58) Khudyakov, I. V.; Serebrennikov, Y. A.; Turro, N. J. *Chem. Rev.* **1993**, *93*, 537–570.

(59) Schmidt, M. W.; Baldrige, K. K.; Boatz, J. A.; Elbert, S. T.; Gordon, M. S.; Jensen, J. H.; Koseki, S.; Matsunaga, N.; Nguyen, K. A.; Su, S.; Windus, T. L.; Dupuis, M.; Montgomery, J. A., Jr. *J. Comput. Chem.* **1993**, *14*, 1347–1363.

(60) Gordon, M. S.; Schmidt, M. W. In *Advances in Electronic Structure Theory: GAMESS a Decade Later*; Dykstra, C. E., Frenking, G., Kim, K. S., Scuseria, G. E., Eds.; Elsevier: Amsterdam, 2005.

(61) Bode, B. M.; Gordon, M. S. *J. Mol. Graphics Modell.* **1998**, *16*, 133–138.

(62) Möller, C.; Plesset, M. S. *Phys. Rev. A* **1934**, *46*, 618–622.

(63) *CRC Handbook of Chemistry and Physics*; Lide, D. R., Ed.; CRC Press: Boca Raton, FL, 2010; Vol. 91.

(64) Jacobs, P. *Group Theory with Applications in Chemical Physics*; Cambridge University Press: Cambridge, U.K., 2005.

(65) Kramers, H. A. *Proc. Acad. Sci. Amsterdam* **1936**, *33*, 959–972.

(66) Dylla, K. G.; Fægri, K. *Introduction to Relativistic Quantum Chemistry*; Oxford University Press: Oxford, U.K., 2007.

(67) Bersuker, I. B.; Polinger, V. Z. *Vibronic Interactions in Molecules and Crystals*; Springer-Verlag: Germany, 1989.

(68) Englman, R. *The Jahn-Teller Effect in Molecules and Crystals*; Wiley-Interscience: London, 1972.

(69) Mironov, V. S.; Ionova, G. V.; Lubimov, V. S.; Groznov, I. N.; Ionov, S. P. *Phys. Status Solidi B* **1981**, *105*, 333–338.